

Preparation of Semiconductor Zinc Oxide Nanoparticles as a Photocatalyst to Get Rid of Organic Dyes Existing Factories in Exchange for Reuse in Suitable Purpose

A. Alhadhrami^{1*}, Abdulraheem S.A. Almalki¹, Abdel Majid A. Adam¹, and Moamen S. Refat^{1,2}

¹Department of Chemistry, Faculty of Science, Taif University, Al-Hawiah, Taif, P.O. Box 888 Zip Code 21974, Saudi Arabia

²Department of Chemistry, Faculty of Science, Port Said University, Port Said, Egypt

*E-mail: msrefat@yahoo.com

Received: 11 March 2018 / Accepted: 19 April 2018 / Published: 5 June 2018

A new photocatalyst zinc(II) oxide (ZnO) was synthesized using a microwave-assisted green method using *p*-hydroxybenzoic acid and zinc nitrate as precursors. The sample was characterized by FTIR, UV-visible, EDX, XRD, SEM and TEM techniques. The molecular formula of the primary precursor [Zn₂(C₇H₅O₃)₂(NO₃)₂(H₂O)₄] binuclear zinc(II) complex was discussed using elemental analyses (CHN), FTIR, UV-visible, XRD, SEM and thermal analysis (TG). This new binuclear complex was formed with *p*-hydroxybenzoic acid as a bridged chelate connecting two zinc metal ions through the carboxylate groups. The chelation assignments declare that Zn(II) metals are coordinated to the *p*-hydroxybenzoate ligand with octahedral geometry. The photocatalytic property of the ZnO products was examined for the degradation of methyl red (MR), methyl orange (MO) and methylene blue (MB) solutions. The resulting data demonstrated a photocatalytic efficiency towards the removal of the selected organic dyes. The Electrical properties of ZnO NPs were measured within the temperature range 313-403 K.

Keywords: ZnO; precursors; organic dyes; XRD; TEM; photocatalyst; electrical properties.

1. INTRODUCTION

Recently, the band gap value of different oxides with semiconductor behaviors, such as zinc(II) oxide [1], In₂O₃ [2], SnO₂ [3] and TiO₂ [4] played an important to identify the photocatalytic properties. These oxides have transport and optical properties that can be used in different modern applications [5-7]. The photocatalytic properties in the presence of visible light were utilized in the degradation of textile dyes, pesticides and pharmaceutical drugs that cause air and water pollution [8–10]. The metal oxides with semiconducting features are highly efficient photocatalysts and can be

functionalized for the removal of toxic and hazardous compounds [11, 12]. The aim of this research is to improve the performance and utilization of nanophotocatalysts in order to enhance the efficiency of advanced oxidation techniques [13]. The photocatalytic activity is dependent on the size and shape of the photocatalyst particles. In recent years, research on the coupling of semiconductor photocatalysts as nanocomposite alloys has been studied to increase the catalytic activity efficiency [14,15]. The photocatalysts have been improved and utilized in the removal of different dyes from industrial wastewaters [16]. The photocatalytic treatment is considered one of the most efficient methods to remove contaminants from water [17]. The photocatalytic activity of ZnO can be improved by controlling the designed shape [18, 19], incorporating other atoms into the lattice [20], increasing the surface area [21] and so on. Transition metal-doped ZnO has attracted the attention of most researchers. Recent investigations on Cu-doped ZnO have reported that Cu exists in the (2⁺) oxidation state in the host lattice [22]. The substitution of Cu into the ZnO lattice improves the photocatalytic activity [23]. Cu-doped ZnO nanopowders have been synthesized by several methods, such as sonochemical [24], sol-gel [25], hydrothermal [26], vapor transport [27], solution combustion [28] and co-precipitation methods [29]. The photocatalytic activities of copper-doped zinc oxides have been investigated by the degradation of methylene blue dye, resazurin dye [22-29] and methyl orange [30].

Access to a clean environment that is free of organic pollutants based on environmentally friendly chemistry is a significant concern. The aim of this research is to prepare nanostructured zinc oxide (ZnO) by using simple and inexpensive organic compounds and a microwave oven as a green method. ZnO was obtained from a metal complex derived from the reaction of *p*-hydroxybenzoic acid and zinc nitrate. The chemical structure of the ZnO product is derived and proven by using different spectral and analytical techniques (microanalytical, FTIR, UV-Vis, ¹H NMR, XRD, SEM, EDX, TEM and thermal analyses). The photocatalytic applications of nanostructured ZnO on the cracking and disposal of dyes contaminants present in wastewater, such as methylene blue (MB), methyl orange (MO) and methyl red (MR) were studied.

2. EXPERIMENTAL

2.1 General

The *p*-hydroxybenzoic acid (Figure 1) and Zn(NO₃)₂·6H₂O were received from Sigma-Aldrich and used as obtained. Ether and ethanol solvents were spectroscopic grade. Elemental analyses of %N, %H and %C were determined using a Perkin Elmer CHN 2400. The zinc metal ion content was obtained using an Atomic Absorption Spectrometer model PYE-UNICAM SP 1900. The molar conductivity of the zinc(II) complex with a 10⁻³ mol/cm³ concentration was obtained with a Jenway 4010 conductivity meter. A UV2–Unicam UV/Vis spectrophotometer was used to record the electronic absorption of the complex dissolved in DMSO solvent (200-800 nm). IR spectra (KBr discs) were measured on a Bruker FT–IR spectrophotometer in the range of 400-4000 cm⁻¹. Thermogravimetric (TG) results were obtained using a Shimadzu computerized thermal analysis system TGA-50H. Samples were separately analyzed under O₂ flow at 30 mL min⁻¹. XRD patterns were collected on an

XPert Philips X-ray diffractometer. The SEM micrographs were visualized using a Jeol Jem–1200 EX II Electron microscope (25 kV). The TEM micrographs were visualized using a JEOL 100s transmission electron microscope.

The d.c. measurements were done with the help of a Source-Measure Unit (Keithley model-236). The a.c. measurements were done on LCZ meter (Keithley model-3330). Platinum was used as contact for all the measurements.

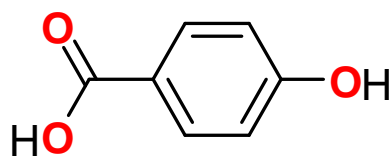


Figure 1. Structure of the *p*-hydroxybenzoic acid.

2.2 Synthesis of the new zinc(II) *p*-hydroxybenzoate complex

Microwave-assisted synthesis, which is a branch of green chemistry has several applications in coordination, organometallic and organic chemistry. This type of synthesis requiring fewer solvents or being solvent-free is very attractive because it offers several benefits, such as high yields, low cost, reduced pollution and simplicity in handling and processing [31, 32]. The zinc(II) *p*-hydroxybenzoate complex was prepared by mixing *p*-hydroxybenzoic acid with $\text{Zn}(\text{NO}_3)_2 \cdot 6\text{H}_2\text{O}$ via 1:2 (metal:ligand) molar ratio at a pH = 8 using 1 N of a NH_4OH solution. A microwave oven was used to irradiate the chemical reaction for 5 minutes using a small amount of ethanol solvent (10 mL). The obtained complex was washed with small amounts of ether and ethanol solvents and then dried under vacuum over anhydrous CaCl_2 .

$[\text{Zn}_2(\text{C}_7\text{H}_5\text{O}_3)_2(\text{NO}_3)_2(\text{H}_2\text{O})_4]$ complex, F. Wt ($\text{C}_{14}\text{H}_{18}\text{N}_2\text{O}_{16}\text{Zn}_2$), M. Wt (601.08 g/mol), Mp. > 250 °C, yield; 85%. Anal.: (Calc.) Found, %: C, (27.97) 27.62; H, (3.02) 2.98; N, (4.66) 4.52; Zn, (21.76) 21.65. $\Lambda_M = 12 \Omega^{-1} \cdot \text{cm}^2 \cdot \text{mol}^{-1}$.

2.3 Synthesis of the ZnO nanoparticles

The ZnO NPs were prepared by calcination of the $[\text{Zn}_2(\text{C}_7\text{H}_5\text{O}_3)_2(\text{NO}_3)_2(\text{H}_2\text{O})_4]$ complex at 600 °C for 2 hours in a static air environment.

2.4 Photocatalytic Activity

The photocatalytic efficiency of the synthesized zinc(II) oxide was assessed by the degradation of a solution containing 20 ppm of each dye dissolved in water. In each experiment, 30 mg of the ZnO photocatalyst was mixed into 30 mL of dissolved dye and stirred for approximately 30 min and then exposed to a UV lamp. A sample solution was collected every 15 minutes, and the absorption was

obtained. The characteristic absorption peaks of the dyes are 528 nm for MR, 464 nm for MO and 613 nm for MB. The degradation efficiency (%) was estimated based on equation No. 1:

$$\text{Degradation efficiency (\%)} = (A_0 - A_t) / A_0 \times 100 = (C_0 - C_t) / C_0 \times 100 \quad (1)$$

where A_t is the absorbance of the dye solution (at a certain reaction time), A_0 is the initial absorbance of the dye solution, C_t is the dye concentration (at certain reaction time), and C_0 is the initial concentration of dye solution.

3. RESULTS AND DISCUSSION

3.1 Characterization of primary precursors zinc(II) complex

The metal carboxylates are an important chemicals in the field of inorganic chemistry and can be used as a model system in bioinorganic chemistry [33]. Metal oxides can be easily synthesized using metal carboxylate as a directly precursors using thermal decomposition methods [34]. The versatile ligational behavior of the carboxylate group can function as a monodentate ligand, a bidentate ligand, or a bridging bidentate ligand [35]. The metal carboxylates chelated with the transition metal ions are attracting attention due to important applications in electrical, magnetic, optical, catalytic, thermal, or biological fields [36]. Figure 2 illustrates the different modes in which carboxylate group can coordinate with metal ions [35].

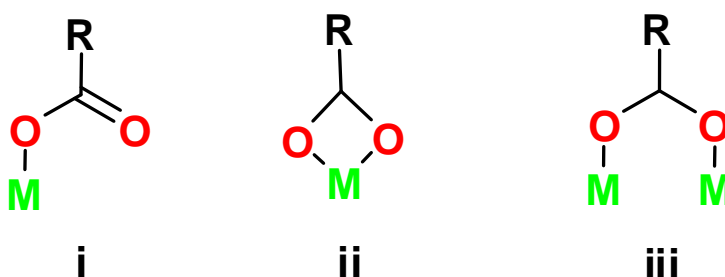


Figure 2. Coordination modes of the carboxylate group.

3.1.1 Microanalytical and conductivity data

The MW, FW, and N, H and C content of the synthesized complex are provided in the experimental section. The microanalytical tool confirmed that the molar ratio was 1:1 (*p*-hydroxybenzoic acid: $\text{Zn}(\text{NO}_3)_2$). The synthesized complex has a white color. The conductance value of the complex dissolved in dimethylsulfoxide solvent with 10^{-3} mol/dm^3 concentration was $12 \Omega^{-1}\text{cm}^{-1}\text{mol}^{-1}$. This value indicates that this complex has a non-electrolytic nature due to the presence of nitrate groups inside the coordination sphere [37].

3.1.2 Infrared spectra

The FTIR spectrum of the zinc(II) *p*-hydroxybenzoate complex (Figure 3) was assigned. The band present at 1694 cm^{-1} in the case of *p*-hydroxybenzoic acid is attributed to the stretching vibration $\nu(\text{C}=\text{O})$ of the COOH group. This band is absent in the spectrum of the synthesized zinc(II) complex and is substituted by two distinguish bands at 1385 and 1621 cm^{-1} due to the symmetric and asymmetric vibrations of the carboxylate group, respectively [38]. The bands observed at 3179 and 3362 cm^{-1} are due to the symmetric and asymmetric O-H stretching modes of the coordinated water molecules, respectively [39]. The difference in frequency, $\Delta\nu(\text{COO})$, between $\nu_{\text{as}}(\text{COO})$ and $\nu_{\text{s}}(\text{COO})$ in the Zn(II) complex is 236 cm^{-1} , which is matched with the sodium salt ($\Delta\nu = 232\text{ cm}^{-1}$). This value suggests that the carboxylate ions appear to be Zn-OO-Zn bridging chelation [38, 39] (Figure 4). The bands at 1097 , 1355 and 1500 cm^{-1} are attributed to the $\nu_{\text{s}}(\text{NO}_2)$ (ν_2), $\nu_{\text{as}}(\text{NO}_2)$ (ν_5) and $\nu(\text{N}=\text{O})$ (ν_1) of the coordinated nitrate group, respectively. These values agree with the characteristic bands of the bidentate chelating nitrate [38, 39]. Mono or bidentate chelating nitrates were differentiated using the separation, $\Delta\nu = \nu_1 - \nu_5$. The increase in $\Delta\nu$ indicates that the coordination changes from mono to bidentate and/or bridging modes. In the synthesized complex, the magnitude of this separation suggests a bidentate chelating nitrate [38]. The separation of the ν_{as} (1621 cm^{-1}) and ν_{s} (1385 cm^{-1}) of the synthesized complex is approximately 236 cm^{-1} , which is matched with the unidentate coordination behavior [38]. The new frequencies that appeared at 503 and 466 cm^{-1} correspond to the $\nu(\text{M}-\text{O})$ stretching vibration.

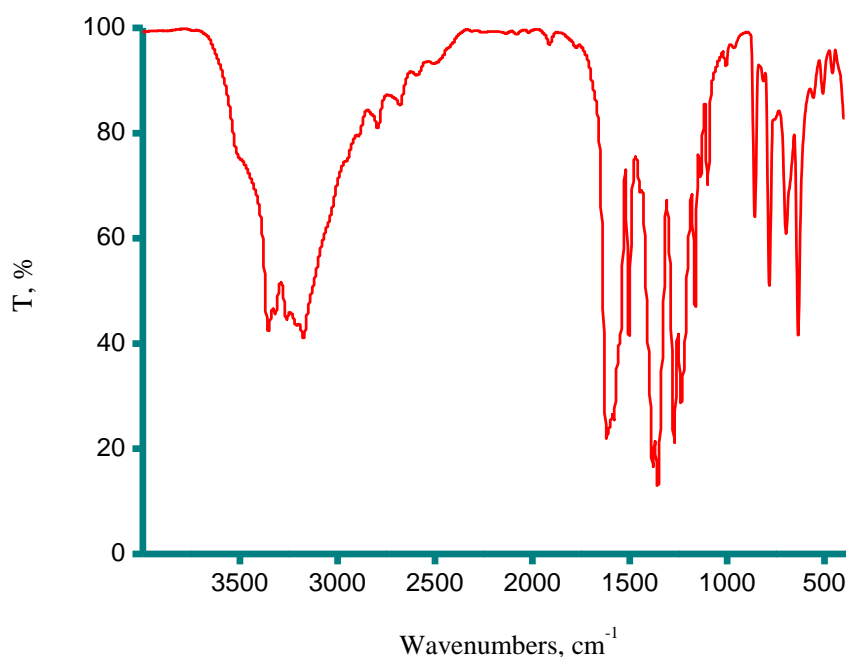


Figure 3. FTIR spectrum of $[\text{Zn}_2(\text{C}_7\text{H}_5\text{O}_3)_2(\text{NO}_3)_2(\text{H}_2\text{O})_4]$ complex.

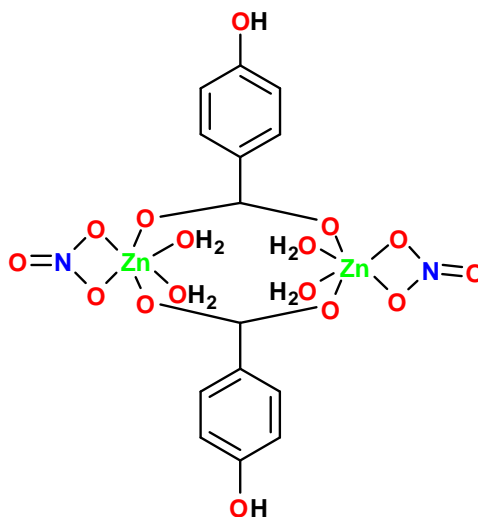


Figure 4. Speculated structure of $[\text{Zn}_2(\text{C}_7\text{H}_5\text{O}_3)_2(\text{NO}_3)_2(\text{H}_2\text{O})_4]$ complex.

3.1.3 UV-Vis spectra

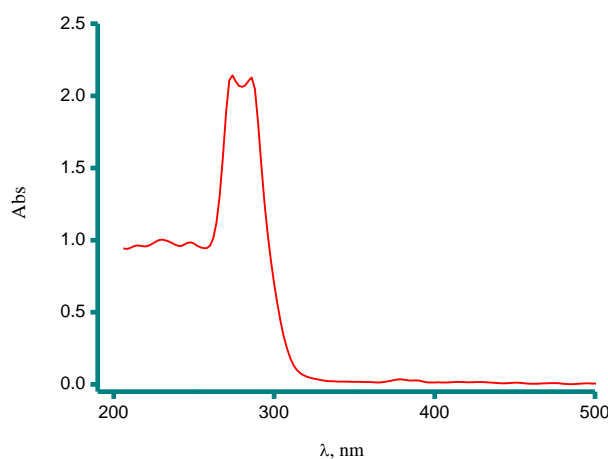


Figure 5. The UV-Vis spectrum of $[\text{Zn}_2(\text{C}_7\text{H}_5\text{O}_3)_2(\text{NO}_3)_2(\text{H}_2\text{O})_4]$ complex.

A UV-Vis spectrum of the zinc(II) *p*-hydroxybenzoate complex is shown in Figure 5. This spectrum was scanned in DMSO with 10^{-3} mol/cm³. The distinguish peaks present at 274 and 286 nm are assigned to the $\pi \rightarrow \pi^*$ electronic transitions, while the peaks located at 378 nm belong to $n \rightarrow \pi^*$ electronic transition. The Zn^{2+} complex is a diamagnetic, as expected for d^{10} systems. Based on the spectral, conductance, and analytical data, the octahedral geometry is suggested as the geometry of the zinc(II) complex [40].

3.1.4 ¹H NMR spectra

The ¹H NMR data (CD₃OD, 400 MHz) of free *p*-hydroxybenzoic acid are δ : 12.4 (1H, s, COOH), 10.2 (1H, s, OH), 7.86 (2H, d, Ar), 6.82 (2H, d, Ar) [41], while the ¹H NMR data (CD₃OD,

400 MHz, Figure 6) of the complex are δ : 6.730, 6.744 (2H, d, Ar), 7.837, 7.851 (2H, d, Ar), 3.383 (8H, s, 4H₂O), 7.977 (1H, s, Ar-OH). In the ¹H NMR spectrum of the complex, the peak at $\delta = 3.383$ ppm is assigned to the proton of the coordinated water molecules, and the singlet at $\delta = 7.977$ ppm is assigned to the proton of the phenolic –OH group, this means that the Ar-OH group does not participate in complexation.

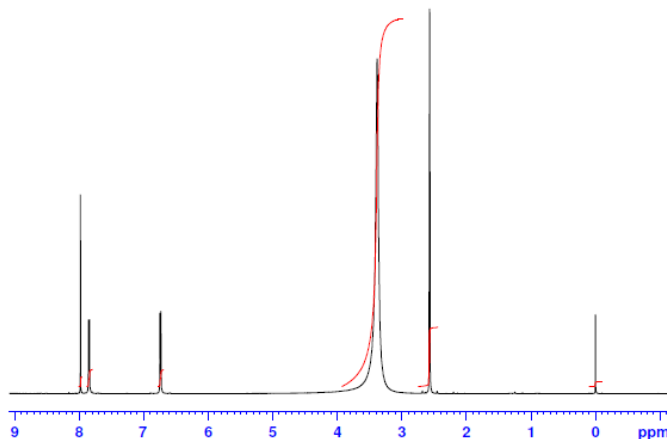


Figure 6. ¹H NMR spectrum of [Zn₂(C₇H₅O₃)₂(NO₃)₂(H₂O)₄] complex.

3.1.5 Thermal analysis and kinetic thermodynamic studies

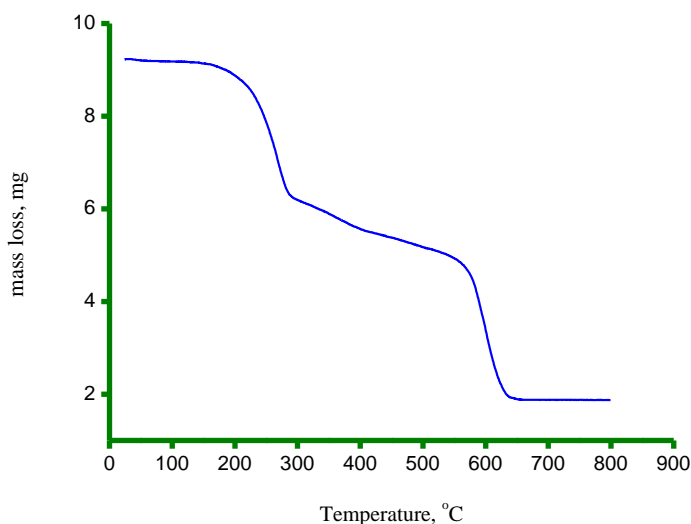


Figure 7. TG curve of [Zn₂(C₇H₅O₃)₂(NO₃)₂(H₂O)₄] complex.

The thermal decomposition of the synthetic [Zn₂(C₇H₅O₃)₂(NO₃)₂(H₂O)₄] complex is scanned within a temperature range of 30-800 °C as shown in Figure 7. The pyrolysis of the Zn(II) complex occurs through three degradation steps. The first step is from 30-300 °C is ascribed to the dehydration of four coordinated water molecules and two nitrate groups with an experimental value of 32.50%, which agrees with the theoretical value 32.61%. The last two steps within the temperature range 300-

650 °C are assigned to the thermal decomposition of both *p*-hydroxybenzoate moieties. The residual as a final product corresponds to the formation of ZnO, which is confirmed by the infrared spectra. The kinetic thermodynamic parameters were theoretically estimated by the integral Horowitz-Metzger (HM) and Coats-Redfern methods [42, 43] (Table 1). The relationships used are: $\Delta G = \Delta H - T\Delta S$, $\Delta S = R[\ln(Ah/kT)]$, and $\Delta H = E - RT$; where h is Planck's constant, and k is Boltzmann's constant. The correlation coefficients of the Arrhenius plots of the degradation steps were in the range of 0.98-0.99, demonstrating a good fit with a linear function. The thermal decomposition process of the zinc(II) complex was non-spontaneous, indicating the thermal stability of the complex [44].

Table 1. Kinetic parameters derived using Horowitz-Metzger (HM) and Coats-Redfern (CR) methods ($\Delta G/\text{kJmol}^{-1}$, $\Delta H/\text{kJmol}^{-1}$, $\Delta S/\text{Jmol}^{-1}\text{K}^{-1}$, Z/s^{-1} , E/kJmol^{-1}).

HM method					CR method				
E	Z	ΔS	ΔH	ΔG	E	Z	ΔS	ΔH	ΔG
101	2.32E+06	-97	98	100	91	4.21E+07	-118	87	121

3.1.6 XRD and SEM studies

Figure 8 shows the XRD patterns of the synthesized zinc(II) *p*-hydroxybenzoate complex. This spectrum shows a diffraction pattern with many peaks ($2\theta = 9.69, 10.62, 12.07, 16.28, 18.31, 19.21, 21.42, 24.35, 26.00, 27.83, 30.21, 31.31, 33.52, 39.02, 40.85, 45.97, 51.28$ and 54.40). The spectrum shows sharp intense peaks, indicating the crystalline nature of the synthesized complex [45]. The spectrum displays distinguished intense peaks at $2\theta = 33.52, 39.02, 45.97$ and 54.40 , which are attributed to the [002], [100], [101], and [102] crystal planes, respectively, for the zinc metal ions. The particle size of the synthesized complex was calculated using the Debye-Scherrer equation (2) [45, 46]:

$$D = K\lambda/\beta\text{Cos}\theta \quad (2)$$

where θ is the Bragg diffraction angle, K is a constant (0.94 for Cu grid), β is the integral peak width, λ is the X-ray wavelength (1.5406 \AA), and D is the particle size. The average particles size calculated for the complex is 30 nm. This value demonstrates that the particle size is located within the nanoscale range. The SEM micrograph of the zinc(II) complex at a 20,000x magnitude is presented in Figure 9. It has been clearly observed that the starting zinc(II) complex in powder form was made of large-to-medium block slices of different sizes. The micrograph indicates that the complex has a clear homogeneous phase.

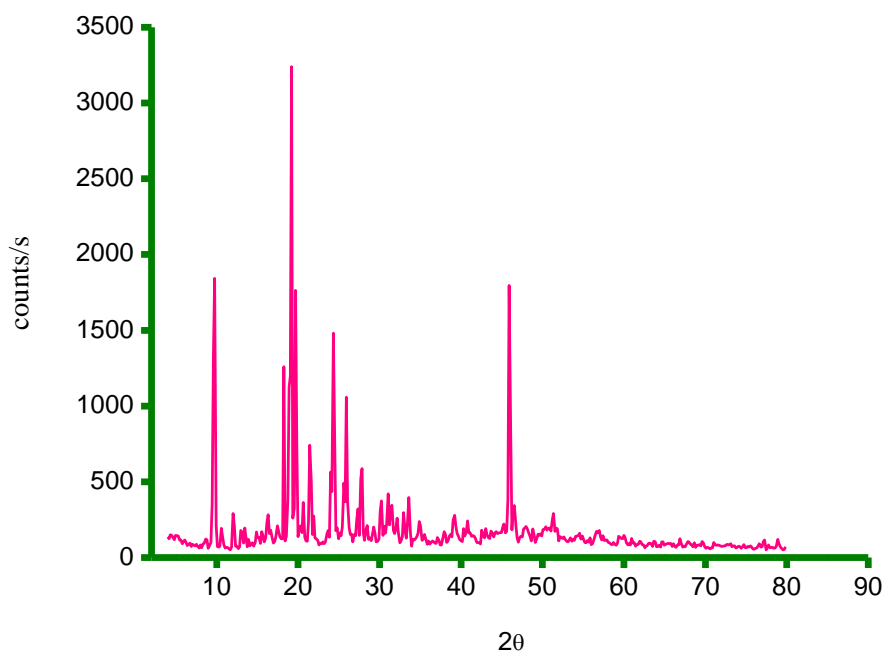


Figure 8. XRD diffraction patterns of $[Zn_2(C_7H_5O_3)_2(NO_3)_2(H_2O)_4]$ complex.

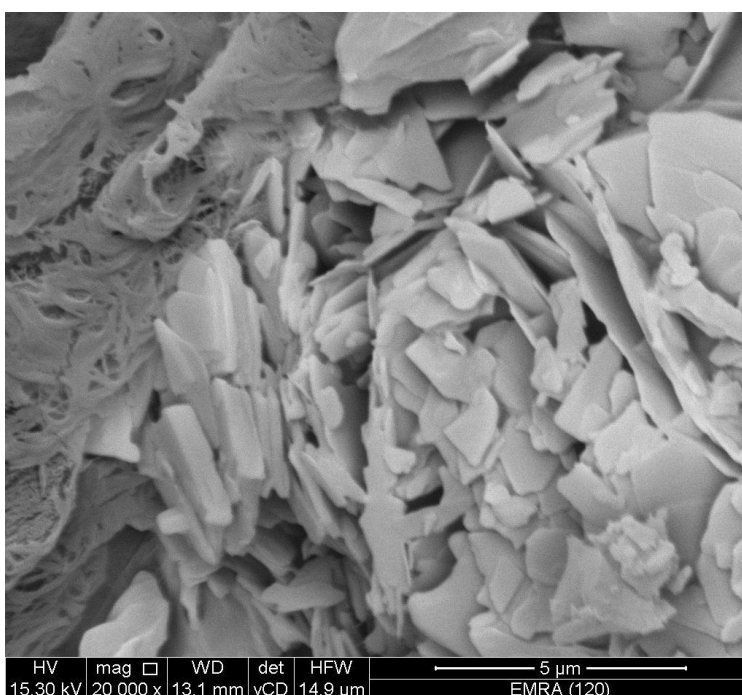


Figure 9. SEM micrograph of $[Zn_2(C_7H_5O_3)_2(NO_3)_2(H_2O)_4]$ complex.

3.2 Characterization of the ZnO NPs

The ZnO nanophotocatalyst was synthesized by a modified precipitation method in which the reaction was carried out in a scientific microwave oven using an ethanol solvent as a green medium.

Then, it was characterized by FTIR, UV-Vis, XRD, SEM-EDX and TEM analyses. The TEM analysis was done to study the particle size and the ZnO nanoparticle morphology was identified based on the analyses of the XRD spectrum and TEM image.

3.2.1 Spectral properties

Figure 10 shows the IR spectrum of the synthesized ZnO with the wurtzite structure. The absorption band observed at 448 cm^{-1} is attributed to the stretching vibration of $\nu(\text{Zn-O})$ of the ZnO nanoparticle material [47]. The medium broad and medium bands at 3291 , 1041 and 664 cm^{-1} can be attributed to the O-H modes of the hydrated water molecules. Figure 11 shows the UV-Vis spectrum of the synthesized ZnO NPs, which was scanned as a dispersed powder form in ethanol. Clearly, a sharp absorption band in the UV region at 400 nm is shown. This band is attributed to the absorption band of the hexagonal wurtzite ZnO NPs [48]. The sharp absorption band (400 nm) decreased, which was attributed to the increased crystallinity of the ZnO sample. The energy band gap of the ZnO NP material was derived using a Tauc plot (equation No. 3) [49]:

$$\alpha h\nu = A(h\nu - E_g)^n \quad (3)$$

where A is a constant, $h\nu$ is the photon energy, E_g is the energy gap, and $n = \frac{1}{2}$ for the allowed direct transition. From Figure 12, the band gap value of the synthesized ZnO is equal to 5.05 eV . This wide band gap (5.05 eV) indicates the semiconductive nature of ZnO, which makes it an excellent material with multifunctional applications in photocatalysts, sensors, and electronics [50, 51].

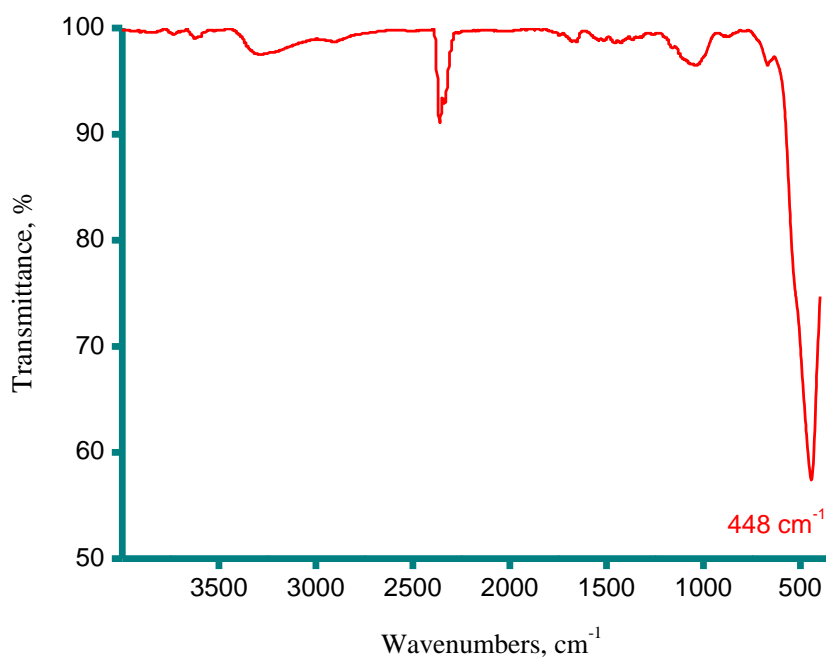


Figure 10. FTIR spectrum of the ZnO nanoparticles.

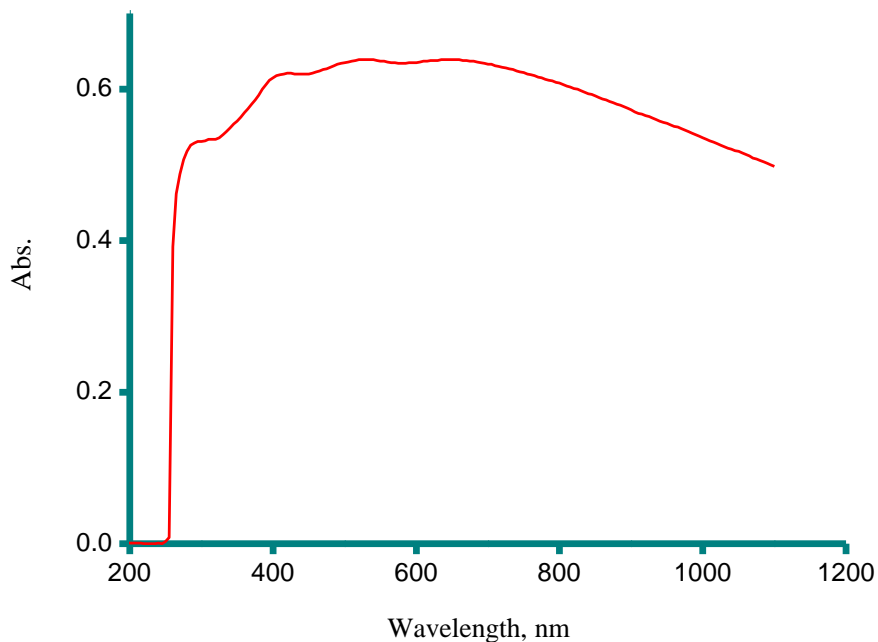


Figure 11. UV-Vis spectrum of the ZnO nanoparticles.

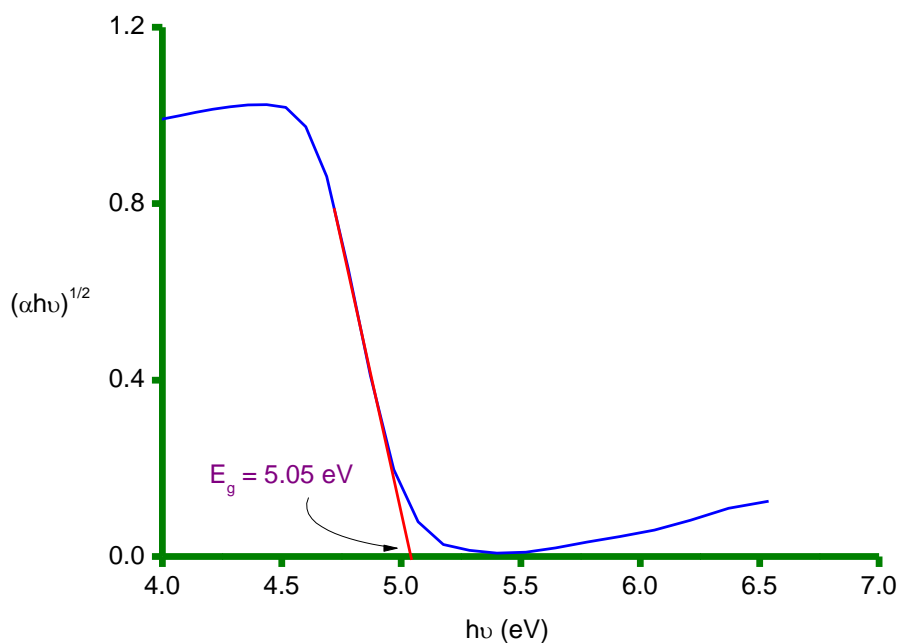


Figure 12. Optical energy band gap plot of the ZnO nanoparticles.

3.2.2 XRD and EDX spectra

Figure 13 show the XRD diffraction patterns of the synthesized ZnO NPs resulting from the thermal decomposition procedure of the zinc(II) *p*-hydroxybenzoate complex. This figure includes the

well-defined diffraction pattern of ZnO, and these patterns exhibited at 56.56° , 47.57° , 36.26° , 34.48° , and 31.81° are attributed to the lattice planes of (110), (102), (101), (002), and (100), respectively. The XRD results refer to the hexagonal wurtzite structure of ZnO (JCPDS 36-1451) [52]. The presence of the characteristic diffraction patterns for ZnO confirms that the complex was completely transformed to zinc oxide. The particle size of the ZnO NPs was calculated using the Debye-Scherrer equation based on the peak at $2\theta = 36.26^\circ$. The average particles size calculated for the ZnO NPs was 45 nm. Figure 14 shows the EDX spectrum obtained for ZnO, which illustrates the elemental and atomic composition of the sample. The spectrum shows the presence of Zn and O without any other impurities.

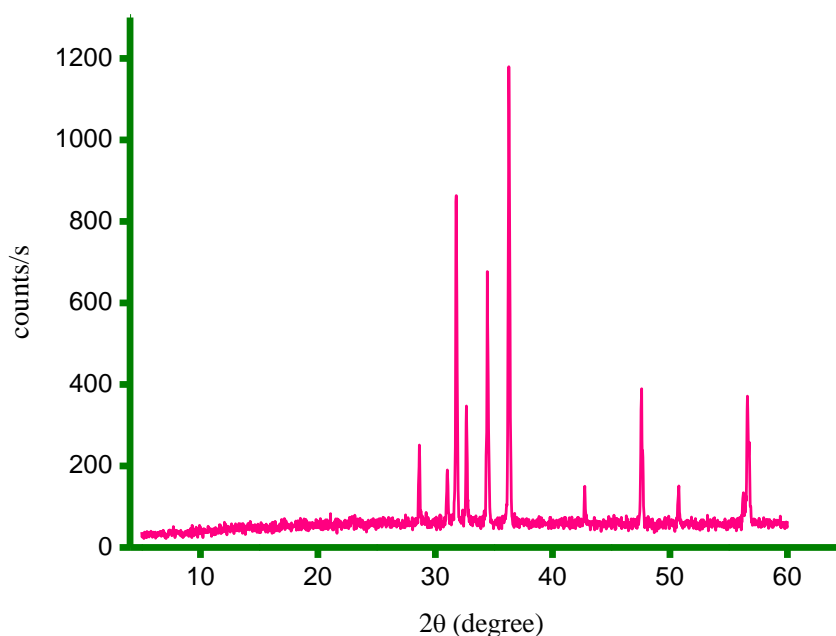


Figure 13. XRD spectrum of the ZnO nanoparticles.

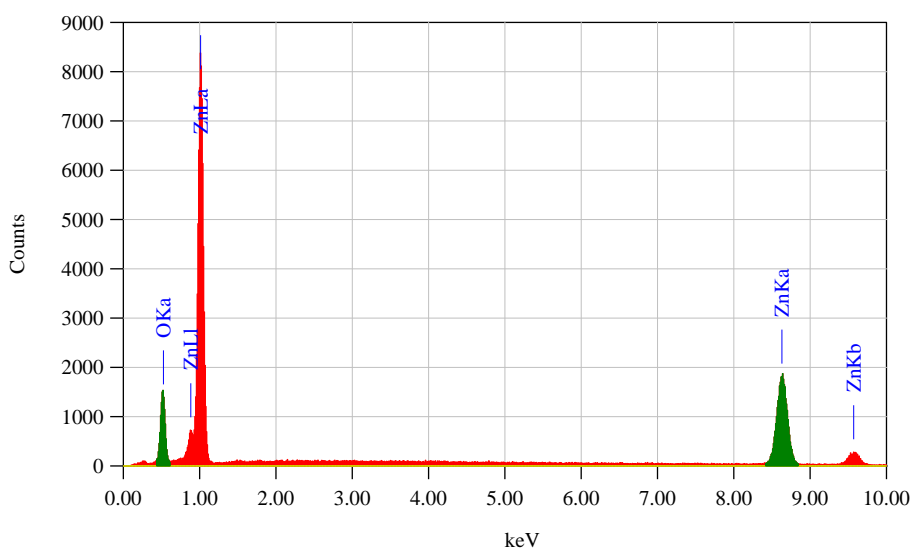


Figure 14. EDX spectrum of the ZnO nanoparticles.

3.2.3 SEM and TEM morphologies

The SEM micrograph of the ZnO sample is shown in Figure 15. The micrograph reveals that the ZnO particles are hexagonal with a granular nature. This high-resolution micrograph with 30- μm magnification illustrates the agglomeration of particles. The SEM image shows a hexagonal feature that agrees with the XRD interpretation of the data. The TEM micrograph of the synthesized ZnO NPs is shown in Figure 16, in which most of the bare ZnO nanoparticles are spherical, and their diameter is ~ 40 nm. This result is in accordance with the value calculated from the X-ray diffraction.

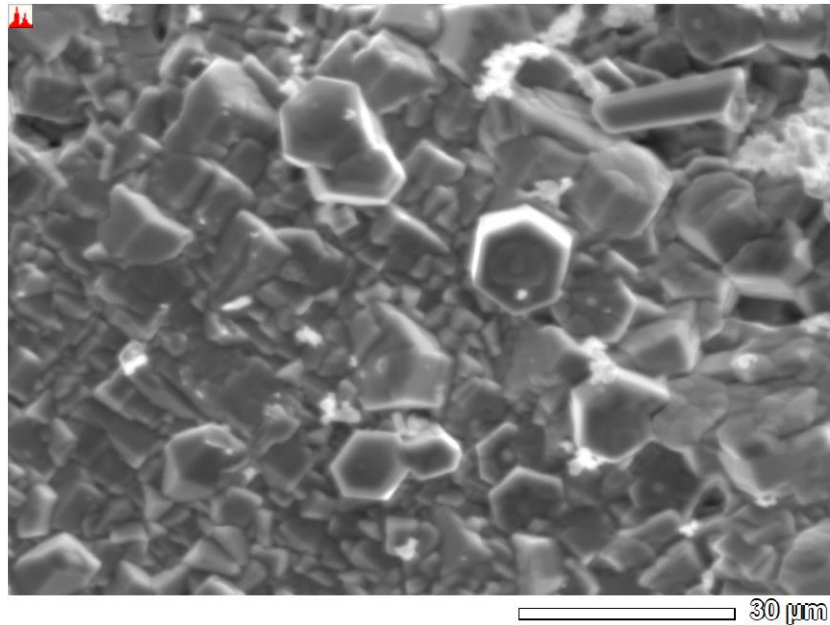


Figure 15. SEM micrograph of the ZnO nanoparticles.

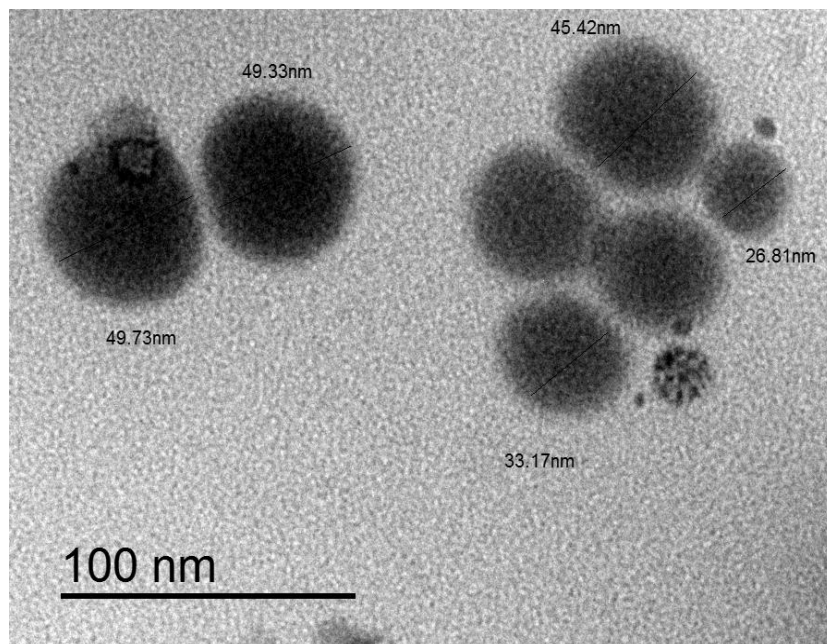


Figure 16. TEM micrograph of the ZnO nanoparticles.

3.3 Photocatalyst applications

Figures 17, 18, and 19 show the time-dependent UV-Vis spectra of the three different dye solutions, namely, the MB, MR, and MO solutions, respectively, during ultraviolet irradiation in the presence of ZnO NPs over 75 min of irradiation. The synthesized ZnO NPs powders can be used as a photocatalyst for the degradation of MO, MR and MB dyes, and they have been adopted as a model photocatalyst compound. In this study, the ZnO NPs catalyst was prepared using a zinc(II) *p*-hydroxybenzoate complex as a precursor. The ZnO NP catalyst with nanoparticle morphology can be used as a model to treat wastewater pollution. The ZnO NPs photocatalytic results confirm that the degradation of the dyes after 75 min of ultraviolet irradiation reached as high as 94.67%, 94.37%, and 93.77% for the MO, MR and MB, respectively. The formation of a nanostructured zinc oxide catalyst increases the degradation efficiency of the dyes. The photocatalytic activity of the synthesized ZnO nanostructure was discussed by assessing the degradation of the MO, MR and MB dyes. The plot in Figure 20 shows the degradation of the three dyes as a function of the duration of UV exposure. The decomposition rates of the three dyes were higher than 90% over 75 min. Based on the mechanism of the semiconducting photocatalyst behavior, the irradiation of this catalyst has a supra-band-gap energy resulting in the association of photo-generated electron-hole pairs. These pairs thereafter spread to the surface, where the electrons adsorbed hydroxide, the hole, and oxygen molecules, to form a hydroxyl radical. Before the holes and the electrons form at the surface, a significant chance in recombination exists [53, 54].

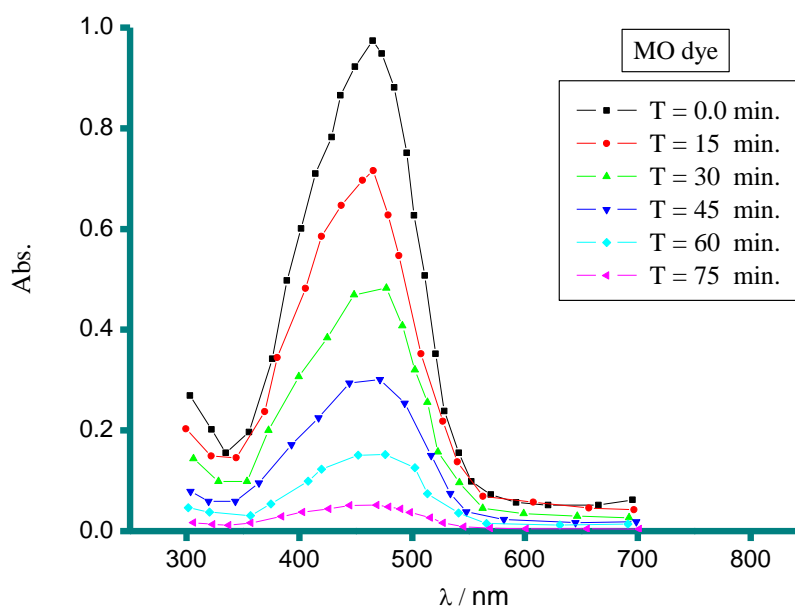


Figure 17. UV-Vis absorption spectrum of MO in the presence of ZnO NPs at different duration time of UV-exposure.

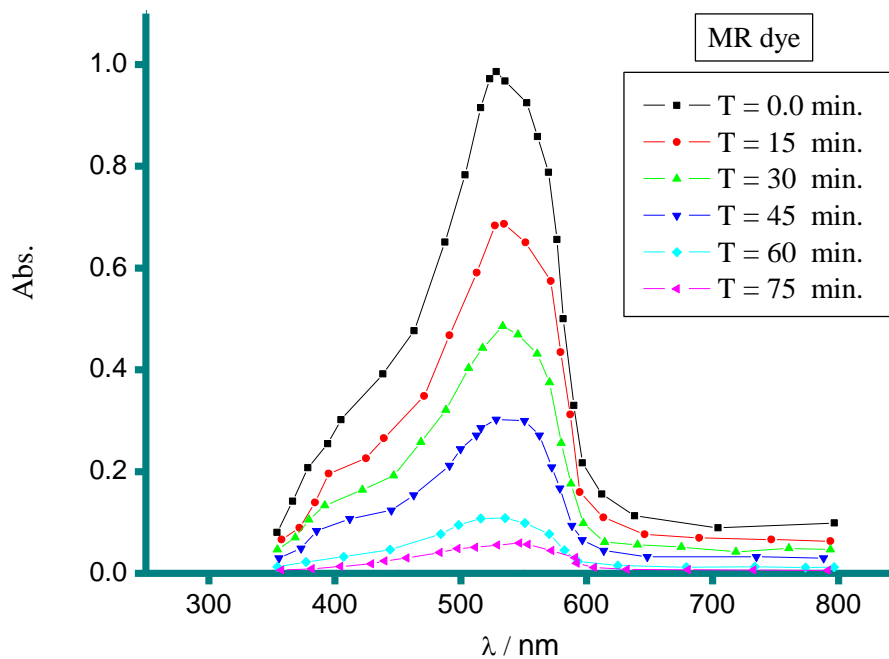


Figure 18. UV-Vis absorption spectrum of MR in the presence of ZnO NPs at different duration time of UV-exposure.

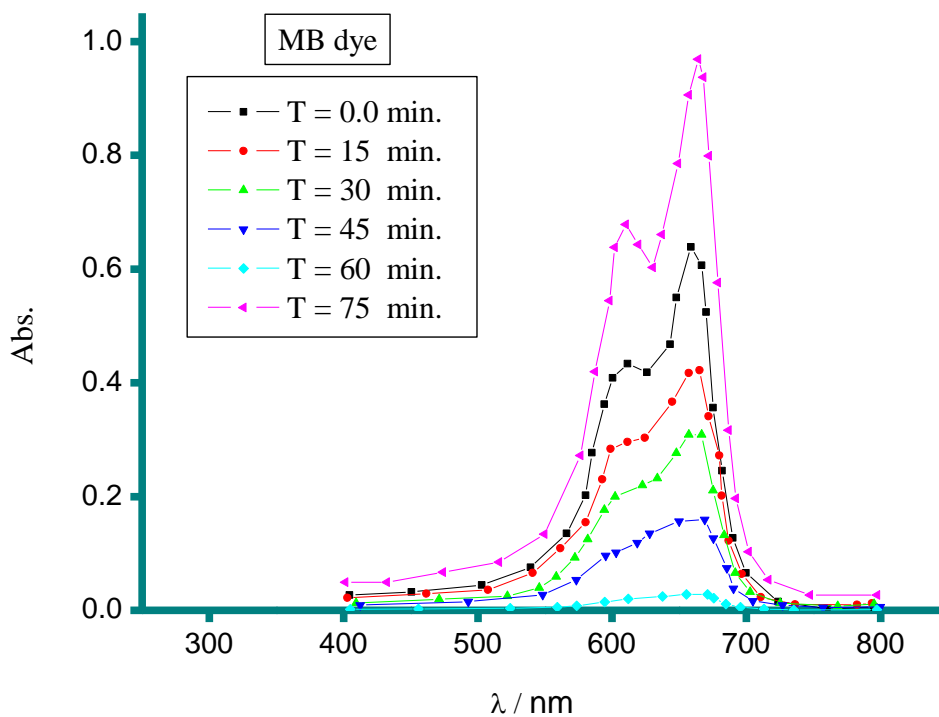


Figure 19. UV-Vis absorption spectrum of MB in the presence of ZnO NPs at different duration time of UV-exposure.

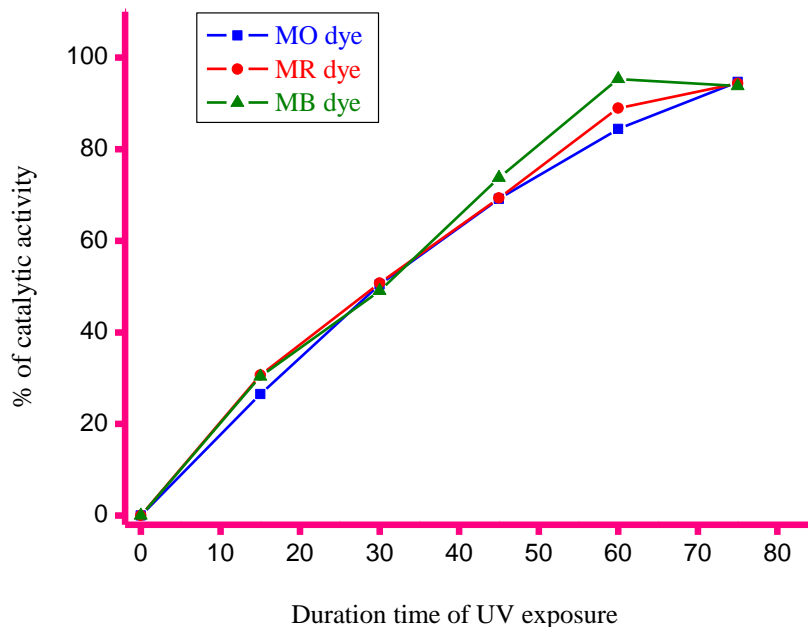


Figure 20. Photodegradation of MO, MR and MB dye using ZnO NPs at duration time of UV exposure.

3.4 Electrical properties

The electrical properties are dependent on various parameters such as composition, thickness, and substrate temperature and deposition rate. For photovoltaic application, important properties include electrical resistivity [55].

The ZnO nanoparticles was compressed in pellet form to measure the d.c. electrical conductivity. The temperature dependence of the d.c. electrical conductivity (σ) of the ZnO NPs was carried out in the temperature range 313-403 K using two probe methods. It was found that the values of σ increase with increasing the temperature according to the Arrhenius relation.

$$\sigma = \sigma_0 \exp(-E_a/KT)$$

Where E_a is the activation energy of the conduction process and σ_0 is constant, K Boltzmann constant and T is the absolute temperature. Figure 21 display the relationship between the different temperature and logarithmic function data of resistivity (ρ). The summarized data listed in (Table 2) give a good impression of the semiconducting behavior of synthesized ZnO NPs [56]. Linear behavior of graph (Fig. 21) shows that the film resistivity is in good agreement with the Arrhenius relation. The activation energy of synthesized ZnO NPs calculated from slope of the graph is 1.31 eV which is agreement with the reported values of activation energy of ZnO [57]. Thus, we can say that zinc oxide is promising materials for temperature sensing. The straight line plot (Fig. 20) suggests that grain boundary limited conduction is the dominant conduction mechanism. The grain boundaries are a consequence of imperfections associated with the polycrystalline nature of the films.

Table 2. Relationship between variable voltage and temperatures

Temperatures/T	Voltage/V	Resistivity/ ρ	$1/T \times 10^{-3}$	$\log \rho$
313	56.4	18.4	3.19	1.26
323	51.7	16.1	3.10	1.21
333	37.2	12.4	3.00	1.09
343	28.3	8.5	2.92	0.93
353	20.5	6.2	2.83	0.79
363	15.9	5.3	2.75	0.72
373	12.1	4.1	2.68	0.61
383	8.6	3.4	2.61	0.53
393	6.8	3.1	2.54	0.49
403	4.1	2.2	2.48	0.34

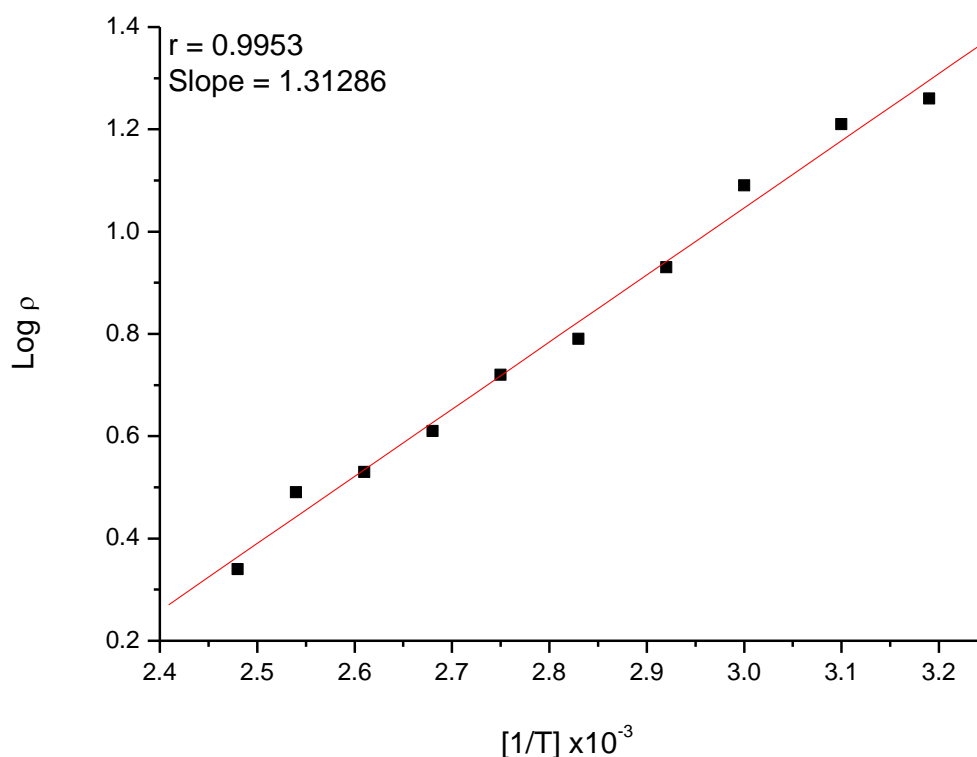


Figure 21. The relationship between temperature dependence and electrical resistivity of ZnO NPs

4. CONCLUSION

The research project demonstrates the practical application of simple and cheap methods for the water purification and desalination companies as well as the institutions responsible for preparing environmental reports and eliminating pigments in the water for the disposal of factories. Herein, this paper was aimed to synthesis and characterization of a new complex of zinc(II) with *p*-hydroxybenzoic

acid; $[\text{Zn}_2(\text{C}_7\text{H}_5\text{O}_3)_2(\text{NO}_3)_2(\text{H}_2\text{O})_4]$. The results suggest that the *p*-hydroxybenzoic acid acts as a bridged chelate towards two zinc metal ions through the carboxylate groups. The nanostructured ZnO material with promising catalytic properties was successfully prepared in air via the controlled thermal decomposition of the synthesized Zn(II) complexes, and it was tested as a catalyst for the heterogeneous degradation of MB, MO, and MR dyes. The XRF analysis confirmed the hexagonal wurtzite structure of ZnO, while TEM analysis confirmed that most of the bare ZnO nanoparticles were spherical and their diameter was approximately ~ 40 nm. The catalytic degradation of the dyes (MR, MO, or MB) in the presence of ZnO as a catalyst was studied at room temperature in water. The results showed that the ZnO product could effectively degrade more than 93% of the investigated dyes. It has been observed that activation energy of ZnO comes out to be 1.31 eV. The conduction in ZnO is through thermally activated process with semiconducting behavior.

ACKNOWLEDGEMENTS

This work was supported by grants from the Vice President for Graduate Study and Research, Taif University, Saudi Arabia under project Grants No. 6008-438-1.

References

1. Y.F. Zhu, D.H. Fan, Y.W. Dong and G.H. Zhou, *Superlattices Microstruct.*, 74 (2014) 261.
2. S. Wang, Y. Zhang, J. Yu, X. Song, Sh. Ge and M. Yan, *Sens. Actuat. B: Chem.*, 891 (2012) 171.
3. J. Tawale, G. Gupta, A. Mohan, A. Kumar and A. Srivastava, *Sens. Actuat. B: Chem.*, 201 (2014) 369.
4. V. Belessi, D. Petridis, *The Role of Colloidal Systems in Environmental Protection*, (2014) 289. <https://doi.org/10.1016/B978-0-444-63283-8.00013-2>
5. P. Hua-Feng, *J. Lumin.*, 182 (2017) 8.
6. O. Almamoun and S.Y. Ma, *Mat. Lett.*, 199 (2017) 172.
7. F. Bensouici, M. Bououdina, A.A. Dakhel, R. Tala-Ighil, M. Tounane, A. Iratni, T. Souier, S. Liu and W. Cai, *Appl. Surf. Sci.*, 395 (2017) 110.
8. Y. Wang, S. Xue, P. Xie, Z. Gao and R. Zou, *Mat. Lett.*, 192 (2017) 76.
9. G. Elango and S.M. Roopan, *J. Photochem. Photobiol. B: Biol.*, 155 (2016) 34.
10. P. Zhou, Y. Xie, J. Fang, Y. Ling, C. Yu, X. Liu, Y. Dai, Y. Qin and D. Zhou, *Chemosphere*, 178 (2017) 1.
11. V.N. Blaskov, I.D. Stambolova and S.V. Vassilev, *Bulgarian Chem. Commun.*, 45 (2013) 263.
12. H. Hagiwara, M. Nagatomo, C. Seto, S. Ida and T. Ishihara, *J. Photochem. Photobiol. A*, 272 (2013) 41.
13. L. Cheng and Y. Kang, *J. Alloy Compd.*, 585 (2014) 85.
14. Y. Yu, G. Chen, G. Wang and Z. Lv, *In. J. Hydrogen Energy*, 38 (2013) 1278.
15. X. Pan and Y.-J. Xu, *Appl. Catal. A*, 459 (2013) 34.
16. J. Yun, D. Jin, Y.S. Lee and H.I. Kim, *Mater. Lett.*, 64 (2010) 2431.
17. M. Hoffmann, S. Martin, W. Choi and D. Bahnemann, *Chem. Rev.*, 95 (1995) 69.
18. R. Mohan, K. Krishnamoorthy and S-J. Kim, *Solid State Comm.*, 152 (2012) 375.
19. L.Y. Yang, S.Y. Dong, J.H. Sun, J.L. Feng, Q.H. Wu and S.P. Sun, *J. Hazard. Mater.*, 179 (2010) 438.
20. J. Sun, S. Dong, J. Feng, X. Yin and X. Zhao, *J. Mol. Catal. Chem.*, 335 (2011) 145.
21. W. Chiu, P. Khiew, M. Cloke, D. Isa, T. Tan, S. Radiman, R. Abd-Shukor, M. Hamid, N. Huang, H. Lim and C. Chia, *Chem. Eng. J.*, 158 (2010) 345.

22. T. Heng, S. lau, S. Yu, J. Chen and K. Teng, *J. Magn. Magn. Mater.*, 315 (2007) 107.
23. C. Chien, S. Chiou, G. Gao and Y. Yao, *J. Magn. Magn. Mater.*, 282 (2004) 275.
24. B. Babu, T. Aswani, G.T. Rao, R.J. Stella, B. Jayaraja and R.V. Ravikumar, *J. Magn. Magn. Mater.*, 355 (2014) 76.
25. D. Sahu, N. Panda, B. Acharya and A. Panda, *Ceram. Int.*, 140 (2014) 11041.
26. J. Huang, Y. Dai, C. Gu, Y. Sun and J. liu, *J. Alloy. Comp.*, 575 (2013) 115.
27. S. lam, J. Sin, A. Abdullah and A. Mohamed, *Separ. Purif. Tech.*, 132 (2014) 378.
28. B. Saravanakumar, R. Mohan, K. Thiyagarajan and S-J. Kim, *RSC Advances*, 3(37) (2013) 16646.
29. M. Ashokkumar and S. Muthukumar, *Opt. Mater.*, 37 (2014) 671.
30. M. Ahmad, E. Ahmed, Z.L. Hong, X.L. Jiao, T. Abbas and N.R. Khalid, *Appl. Surf. Sci.*, 285P (2013) 702.
31. K. Mahajan, M. Swami and R.V. Singh, *Russ. J. Coord. Chem.*, 35 (2009) 179.
32. K. Sharma, R. Singh, N. Fahmi and R.V. Singh, *Spectrochim. Acta A*, 75 (2010) 422.
33. V.L. Pecoraro, M.S. Baldwin and A. Gelasco, *Chem. Rev.*, 94 (1994) 807.
34. K.S. Rane and V.M.S. Verenkar, *Bull. Mater. Sci.*, 24 (2001) 39.
35. B.R. Srinivasan and S.C. Sawant, *Thermochim. Acta*, 402 (2003) 45.
36. Y. Chen, C.B. Liu, Y.N. Gong, J.M. Zhong and H.L. Wen, *Polyhedron*, 36(1) (2012) 6.
37. G.B. Deacon and R.J. Phillips, *Coord. Chem. Rev.*, 33 (1980) 227.
38. K. Nakamoto, *Infrared and Raman Spectra of Inorganic and Coordination Compounds*, John-Wiley and Sons, New York, 1997.
39. K. Burger, *Coordination Chemistry: Experimental Methods*, Akademiai Kiadó, Budapest, 1973.
40. Y. Ma and P. Wang, Chemical constituents of the leaves of *Xanthoceras sorbifolia* Bunge [J]. *Chinese Traditional Patent Medicine*, 32(10) (2010) 1750.
41. P.K. Panchal, H.M. Parekh, P.B. Pansuriya and M.N. Patel, *J. Enzyme Inhibit. Med. Chem.*, 21 (2006) 203.
42. A.W. Coats and J.P. Redfern, *Nature*, 201 (1964) 68.
43. H.W. Horowitz and G. Metzger, *Anal. Chem.*, 35 (1963) 1464.
44. A.A. Frost and R.G. Peasron, *Kinetics and Mechanism*, New York: Wiley, 1961.
45. B.D. Cullity, *Elements of X-Ray Diffraction*, Second Edition, Addison-Wesley Publishing Company, 1978, ch. 5.
46. C. Savall, C. Rebere, D. Sylla, M. Gadouleau, Ph. Refait and J. Creus, *Mater. Sci. Engineer A*, 430 (2006) 165.
47. L. Kumari and W.Z. Li, *Cryst. Res. Technol.*, 45(3) (2010) 311.
48. F. Davar, A. Majedi and A. Mirzaei, *J. Am. Ceram. Soc.*, 98(6) (2015) 1739.
49. R. Bhatt, I. Bhaumik, S. Ganesamoorthy, A.K. Karnal, M.K. Swami, H.S. Patel and P.K. Gupta, *Physica Status Solidi A*, 209(1) (2012) 176.
50. H. Morkoc, *Zinc oxide: fundamentals, materials and device technology*, (Weinheim Germany: Willey-VCH), 2007.
51. S. Malato, Proc. IOCD/CYTED Symp. VIII-G 4 pp 79-101.
52. J.E. Jaffe and A.C. Hess, *Phys. Rev. B*, 48 (1993) 7903.
53. C.-W. Tang, *Modern Research in Catalysis*, 2 (2013) 19.
54. H. Gerischer, *Electrochimica Acta*, 38(1) (1993) 3.
55. V. Kumar, M.K. Sharma, J. Gaur and T.P. Sharma, *Chalcogenide lett.*, 5 (2008) 289.
56. M. Kota, F. Dagdelen and Y. Aydogdu, *Mater Lett.*, 58 (2004) 901.
57. H. Watanabe, M. Wada and T. Takahashi, *Japanese J. Appl. Phys.*, 4(12) (1965) 945.